Journal of ELECTRONIC MATERIALS
https://doi.org/10.1007/s11664-020-08244-1
© 2020 The Minerals, Metals & Materials Society

Construction of Z-Scheme CdS/WO_3 Heterostructure on Photonic Crystals with High-Efficiency Photocatalysis Performance

MENGSHI CHEN[1] and YE XIAO[1,2]

1.—School of Materials and Energy, Guangdong University of Technology, Guangzhou 510006, China. 2.—e-mail: yexiao@gdut.edu.cn

Tungsten oxide (WO_3) has been widely used as a photocatalyst for its suitable bandgap and relative stability. However, the high recombination rate of photo-generated carriers impedes raising the photocatalytic efficiency of tungsten oxide (WO_3) beyond its current value. In this work, a cadmium sulfide (CdS) and tungsten oxide (WO_3) Z-scheme heterostructure system was constructed which shows improved photocatalytic performance due to better hole-electron separation. In addition, photonic crystal fluorine-doped SnO_2 (FTO) was applied to the photoanode as a supporting framework for CdS and WO_3, which can also play a role in assisting photocatalytic materials to assimilate light at the same time. As a result, the overall photocatalytic performance of a Z-scheme system on a photonic crystal framework has been significantly increased beyond that of conventional tungsten oxide.

Key words: Photocatalysis, degradation, thin films, heterogeneous catalysis

INTRODUCTION

Due to the increasingly serious environmental pollution and energy shortages, the field of photoelectrochemistry has received more and more interest in its investigation of energy utilization from solar power.[1,2] The photo-anode plays a crucial role in solar energy conversions. Various methods have been developed to increase the photoactivity of the photo-anode, such as building a heterogeneous system,[3,4] doping metal ions,[5] and structuring the photocatalysts.[6,7] A variety of photoactivated materials have been used in the photo-anode, such as TiO_2,[8] g-C_3N_4,[9] and α-Fe_2O_3.[10] To further improve the utilization of photo-induced charges, heterostructures are better suited to tailoring the conduction band minimum and the valence band maximum than the single kind of semiconductor. Therefore, several types of band offset configurations have been applied to prompt the separation of electron–hole pairs, such as type-II band offset configuration.[11,12] Typically, a Z-scheme configuration, which combines two semiconductor materials with suitable band offsets, has attracted much attention in the fields of photocatalysis and photoelectrochemistry. In a Z-scheme system, the photoinduced electrons of the lower conduction band of one semiconductor are transported to the valence band of another semiconductor, and finally, recombine holes. Thus, the change of the surface can participate in the reaction as much as possible. For the above-mentioned reasons, the Z-scheme system efficiently improves the utilization of photo-induced electrons and holes[13] and has a higher redox capacity compared with the conventional type-II system.

The energy level is a crucial requirement to form a Z-scheme structure. Many heterostructure systems have been studied, such as ZnO-CdS,[14] $CaFe_2O_4$-WO_3,[15] CuS-WO_3[16] and g-C_3N_4-WO_3.[17] Among them, the narrow bandgap semiconductor CdS (2.4 eV) has a suitable bandgap width, high conduction band potential and high absorption coefficient.[18,19] However, if the rapidly combined

(Received March 2, 2020; accepted May 27, 2020)

Published online: 04 June 2020

photogenerated electron–hole pairs could be inhibited by constructing them with other semiconductors, the result would be far more exciting. WO_3 has a high valence band potential (versus 3.49 eV) and narrow band gap width (E_g 2.4–2.7 eV), showing excellent photoelectric chemical properties, such as non-toxic, chemical, and optical stability, and thus has been widely studied as a photoelectric anode material.[20–23]

To further improve the light-harvesting and to supply high specific surface area, photonic crystals (PCs) have been used to construct the structural substrates to support photocatalysts.[23] PCs can increase the effective path length of light via multiple scatterings,[24] which enhances the possibility of light absorption and photocatalytic efficiency.[25] Thus, PCs have several advantages in the application of substrates for photocatalysts. Periodic hollow structures have the possibility of manipulated photonic properties. A lower density favors high delivering ability and surface permeability. High surface area provides more photoactive sites. Furthermore, PC film as a template or skeleton may have the dual ability to modify the microstructure of photoactive materials. Based these considerations, FTO is an excellent substrate in the application of photocatalysis[26,27] for its good electrical conductivity, low cost and high chemical stability.

In this work, the system of a WO_3 and CdS composited heterostructure under the support of PCs FTO has been fabricated to utilize the benefits of photonic properties and Z-scheme band offsets. The enhanced photocatalytic performance could be achieved by the efficient separation of photo-generated electrons and holes due to the Z-scheme configuration.[28–30] Because of the high surface area and porous morphology, the efficiency of the photoanode was improved. What is more, the supported bulk framework for the photoactive materials has advantages in the recycling procedures compared with conventional powdery materials, which is beneficial for the large-scale application in wastewater treatment.

EXPERIMENTAL SECTION

Catalyst Preparation

Analytical-grade reagents were used in the experiment without further purification. WCl_6, polystyrene spheres (PS) (500 nm in diameter), NH_4F, $SnCl{\cdot}5H_2O$, ethanol, methyl alcohol, $Cd(AC)_2$ ($Cd(CH_3CO_2)_2$) and $Na_2S{\cdot}9H_2O$ were purchased from Aladdin.

Fabrication of PCs-FTO Substrate

The FTO (1 cm^2) coated electrode was immersed in a PS sphere suspension which was dissolved in ethanol in a glass wide-mouth bottle, and heated in a muffle furnace at 58°C for 15 h until PS sphere film was deposited in the electrode under capillary force with an FCC stacking. After pre-soaking in ethanol for 15 min, the electrode was dipped in the precursor solution for 45 min. The precursor was prepared from $SnCl_4{\cdot}5H_2O$ (1.4 g, 4 mmol/L), which was sonicated in ethanol (20 mL) until dissolved. The saturated NH_4F solution (0.24 g, 2 mmol/L) was then added, and the resulting mixture sonicated until the solution was transparent. The electrode then was transferred to a furnace oven to anneal with the heat ramp of 1°C min^{-1} to 450°C and hold for 2 h in air, thus the fluorine-doped SnO_2 formed as an inverse opal structure with a three-dimensional periodical structure.

The Synthesis of WO_3 in PCs-FTO

The WO_3@PCs-FTO was synthesized by a conventional hydrothermal method. WO_3 precursor solution was prepared by dissolving WCl_6 (0.25 mmol/L) in methanol (20 mL). The PCs-FTO was transferred into a 25 mL Teflon-lined autoclave with 12 mL of WO_3 precursor solution. The autoclave was maintained at 100°C for 12 h. Then the electrodes were transferred into the furnace oven for calcination at 475°C for 2 h in air. Commercially available synthesized WO_3 in planar FTO (WO_3@p-FTO) (1Ω/m^2 sheet resistance) was use as the control.

The Synthesis of CdS-WO_3 Z-Scheme Heterostructure Photocatalysts

The CdS–WO_3 heterostructure photocatalysts were prepared using an in situ approach. The precursor solution of CdS–WO_3 heterostructure was prepared from $Cd(AC)_2$ (0.515 g, 50 mmol/L) and $Na_2S{\cdot}9H_2O$ (0.716 g, 50 mmol/L) dissolved in ethanol (20 mL) and deionized water (20 mL), respectively. After dipping in the $Cd(AC)_2$ solution for 30 s and blowing dry under purified N_2, the WO_3@PCs-FTO was dipped in $Na_2S{\cdot}9H_2O$ solution for 30 s. Excess reagent was removed by washing with DI water. The electrode then was blown dry by purified N_2. The CdS-WO_3@PCs-FTO composites were obtained after the as-prepared samples were transferred to the pipe furnace for heat treatment at 400°C for 30 min with a heat ramp rate of 1°C min^{-1} in N_2.

CHARACTERIZATION

A field emission scanning electron microscope (SEM) (Hitachi */SU8220) was used to measure the morphology of WO_3@PCs-FTO and CdS-WO_3@PCs-FTO. Transmission electron microscopy (Thermo */Talos F200S), high-resolution transmission electron microscopy (HRTEM), and element mappings were conducted with the (*/Talos F200S) transmission electron microscope. The crystalline phase was

obtained by the Bruker D8 advance x-ray diffractometer (XRD). The UV–Vis diffuse reflectance spectrum (UV–Vis DRS) of WO_3@PCs-FTO and CdS-WO_3@PCs-FTO (380–800 nm) was detected on a UV–Vis–NIR spectrophotometer (*/UV-3600 Plus). Photoluminescence spectra analysis was carried out on a fluorescence spectrophotometer (*/Fluorolog-3).

Photoelectrochemical Measurements

Photocurrents were measured using an electrochemical analyzer (CH1660C Instruments) in a standard three-electrode system with as-prepared samples as working electrodes, Pt wire as counter electrode, and Ag/AgCl (saturating KCl) as reference electrode. A 100 mW cm^{-2} xenon lamp was utilized as a visible light source. Na_2SO_3 (0.35 M) and $Na_2S{\cdot}9H_2O$ (0.25 M) mixed solution was used as the electrolyte.

Photo-Degradation Reaction

Photo-degradation reactions were carried out at room temperature under visible light. The concentration of rhodamine B (RhB) solution was 0.1 mmol/L/L. The CdS-WO_3@PCs-FTO in RhB solution was kept in the dark overnight. The solution and the surface of the electrode reached adsorption balance. Its initial absorbency was determined. The photocatalytic reaction was initiated by irradiating with a 100 mW cm^{-2} xenon lamp. Sampling analyses were conducted at 40 min intervals.

RESULTS AND DISCUSSION

Morphology Characteristics

Figure 1a shows SEM images of the as-prepared PCs-FTO products, which reveal the ordered periodic structure of the PCs-FTO electrodes. The thickness of PCs-FTO is about 1.5 μm, which corresponds to 6–7 layers. The estimated surface area is about 21 times larger than a planar substrate, and the arrangement of pores is tight and tidy. Figure 1b and c show the SEM images of the WO_3@PCs-FTO and CdS-WO_3@PCs-FTO. WO_3 particles, which uniformly adhere to or distribute on the PCs-FTO skeleton. The details of the formation mechanism can be seen in the supporting information (Figure S2). The CdS particles cover the skeleton of PCs-FTO and WO_3 particles. To obtain additional information regarding the microstructure of WO_3 and CdS, TEM analysis was performed. The TEM image (Fig. 1d) depicts the CdS-WO_3@PCs-FTO.

Qualitative Analysis

HRTEM image of CdS-WO_3@PCs-FTO (Fig. 2a) reveals WO_3 and CdS are loaded compactly on the framework of PCs-FTO. This intimate contact among SnO_2, WO_3, and CdS facilitates electrons transferring from WO_3 to CdS and then to the external circuit during photoexcitation. The charge separation and photocatalytic efficiency are enhanced. Lattice spacing values were 2.6, 3.35, and 3.7 Å, which correspond to the (101) plane of tetragonal SnO_2, the (111) plane of cubic CdS, and

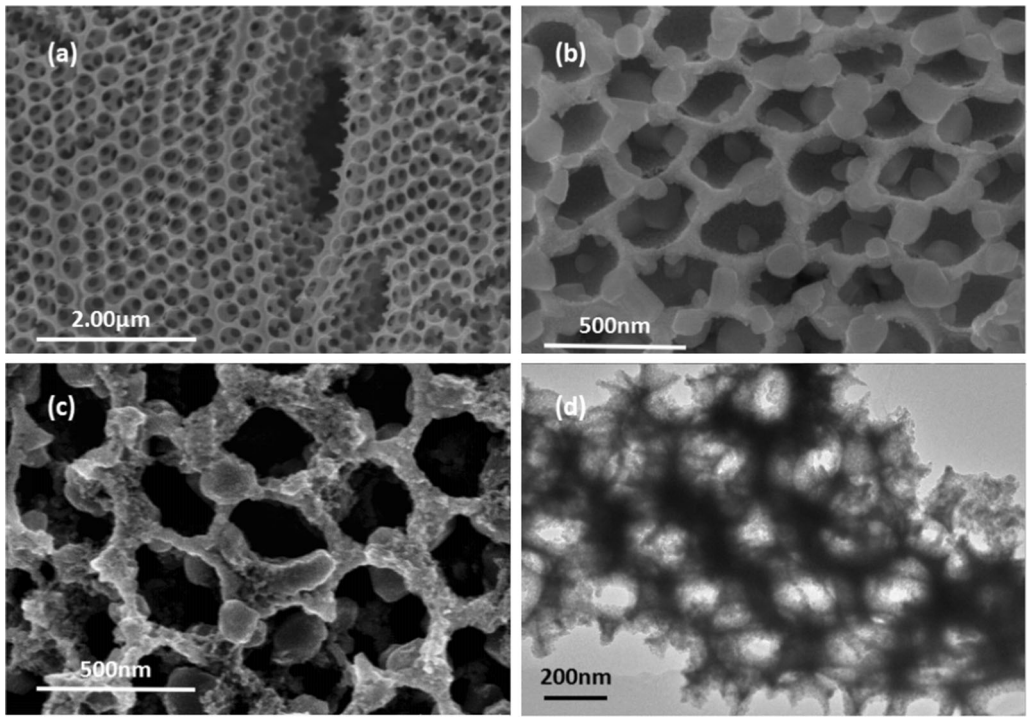

Fig. 1. SEM images of (a) PCs-FTO film, (b) WO_3@PCs-FTO, (c) CdS-WO_3@PCs-FTO; (d) TEM images of CdS-WO_3@PCs-FTO.

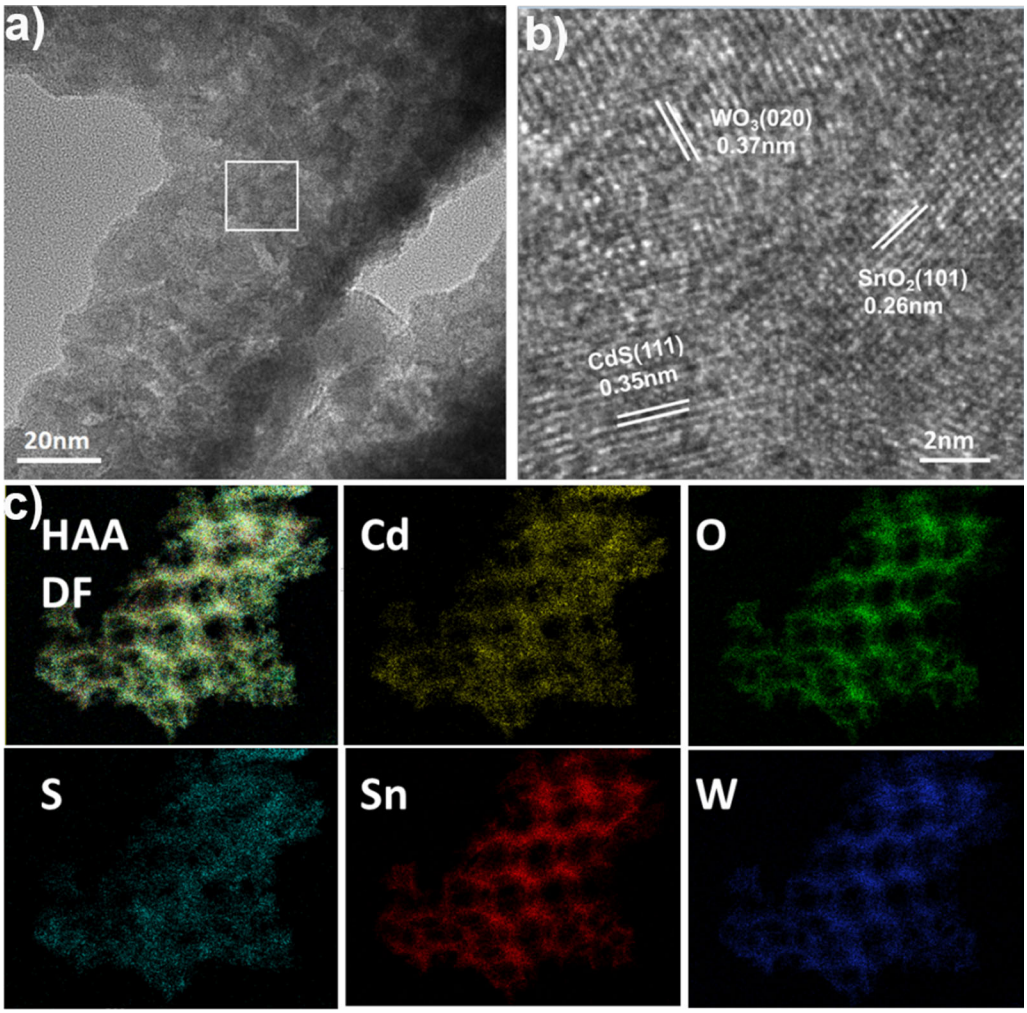

Fig. 2. (a) Image of TEM of CdS-WO_3@PCs-FTO; (b) image of HRTEM of CdS-WO_3@PCs-FTO; (c) EDS mapping of CdS-WO_3@PCs-FTO.

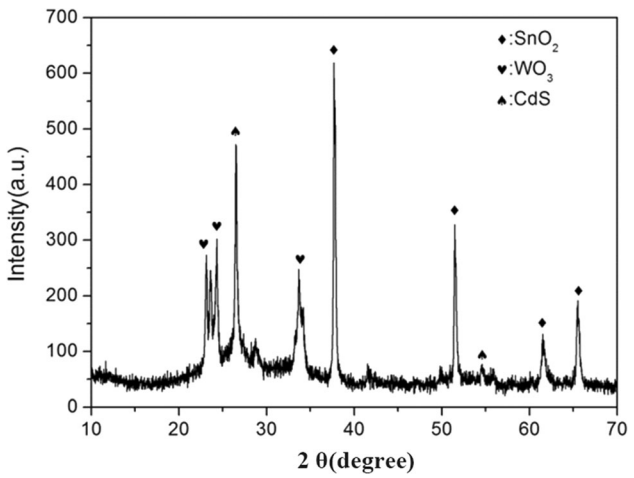

Fig. 3. XRD patterns of CdS-WO_3@PCs-FTO.

the (020) plane of monoclinic WO_3, respectively. EDS mapping images (Fig. 2c, d, e, f, g and h) demonstrated the distribution of W, Cd, S, O, Sn, confirming the uniform distribution of the WO_3 and CdS on the skeleton of SnO_2.

Figure 3 shows the XRD patterns of CdS-WO_3@PCs-FTO. The characteristic diffraction peaks of WO_3 match well with lattice parameters of a = 7.306 Å, b = 7.54 Å, and c = 7.692 Å (JCPDS No. 72-0677). SnO_2 matches with lattice parameters of a = 4.746 Å, b = 4.746 Å and c = 3.193 Å (JCPDS NO. 77-0450). CdS matcsed with lattice parameters of a = 5.830 Å, b = 5.830 Å, and c = 5.830 Å (JCPDS NO. 89-0440). Characteristic diffraction peaks of CdS were weaker than WO_3 and SnO_2 because of the relatively low volume fraction. In addition, the peak of CdS overlaps the peak of SnO_2 at 26°. No significant shift in peak positions was observed, indicating that CdS was not incorporated into the lattice of WO_3.

UV–Vis Diffuse Reflectance Spectra

The black line and red line in Fig. 4 show the absorption of WO_3@PCs-FTO and CdS-WO_3@PCs-FTO, respectively. The absorption of WO_3@PCs-FTO was rapidly improved at a wavelength of < 500 nm because of its intrinsic bandgap absorption of anorthic WO_3(2.5 eV). Compared with the black

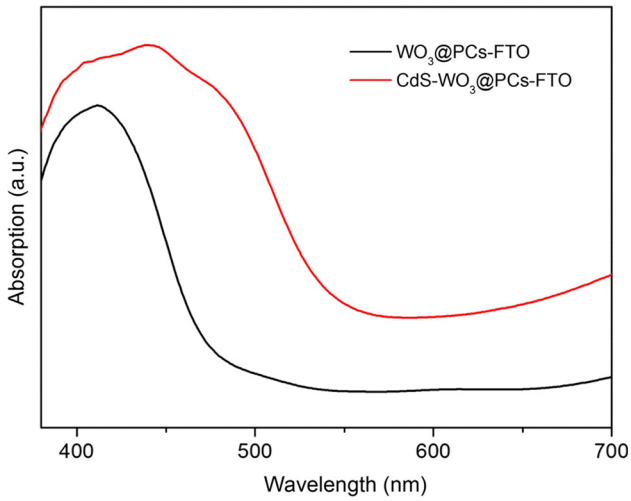

Fig. 4. UV–Vis diffuse reflectance spectra of WO_3@PCs-FTO and CdS-WO_3@PCs-FTO.

line, the range of absorption of the red line was wider because of the intrinsic bandgap absorption of cubic CdS (2.3 eV). The absorption of CdS-WO_3@PCs-FTO was significantly improved at wavelengths from 380 nm to 550 nm. The long-range ordered arrays of macroporous materials possess periodic modulation of refractive index (RI) on the length scale of optical wavelength. The material, external media, and periodicity differences of RI lead to the formation of a photonic stop band (PSB). The PSB inhibits the propagation of photons and causes multiple scattering within a particular wavelength, which satisfies Bragg-Snell's law. These effects enhance the light absorption for embedded photoactive materials.[31] The reflection at the stopband maximum wavelength (λ_{max}) can be estimated by the following equations:

$$\lambda_{max} = \frac{2d_{hkl}}{m}[\varphi n_w^2 + (1-\varphi)n_{void}^2 - \sin\theta^2]^{1/2}, \quad (1)$$

$$d_{hkl} = \frac{D\sqrt{2}}{\sqrt{h^2+k^2+l^2}}, \quad (2)$$

where n_w is the RI of FTO and n_{void} is the RI of air, D is the diameter of the spheres, m is the Bragg lattice order, which is unity in this case, ϕ is a filling factor, which could be considered as about 26%. As a result, the peak of the PSB is about 486 nm. Due to a common broadening effect of the light absorption and slight deviation from this idealized model, light absorption is improved in the 380–550 nm range.

Photocatalytic Activity

Z-scheme CdS/WO_3-based composites with excellent photocatalysis have been reported and the transfer mechanism of photoexcited charge carriers has been studied comprehensively.[28–30] The physical mechanism of photocatalytic reaction and diffusion process of photoexcited electrons and holes of the CdS-WO_3 heterostructure are illustrated in Fig. 5. The conduction band minimum (CBM) of CdS (− 0.6 eV)[32] is more negative than that of WO_3 (0.5 eV)[15] and the valence band maximum (VBM) of WO_3 (3.0 eV) is more positive than that of CdS (1.7 eV). In the Z–scheme charge transfer mechanism, the photoinduced electrons in the CBM of WO_3 migrate to the VBM of CdS, and a fast combination is achieved. Thus, the electrons accumulated in the CBM of CdS have more negative potential and the holes accumulated in VBM of WO_3 has more positive potential, indicating excellent photocatalytic performance.

The photocatalytic characteristics of the as-fabricated composite were estimated by detecting the transient photocurrent responses under full-spectrum light on/off cycles. It is effective to qualitatively study the excitation and transfer of photoinduced electrons and photoinduced holes. Figure 6 shows a comparison of the photocurrent–time (I–t) curves of WO_3@p-FTO, WO_3@PCs-FTO, PCs-FTO, CdS-WO_3@PCs-FTO, and CdS-WO_3@p-FTO electrodes. It was clear that photocurrent observed in all electrodes exhibited a fast and reproducible photocurrent response in on/off cycles of visible light irradiation. The photocurrent of the CdS-WO_3@PCs-FTO electrode was about 5 times higher than that of the WO_3@p-FTO, about 3 times higher than that of the WO_3@PCs-FTO, and about 2 times higher than that of the CdS-WO_3@p-FTO (Fig. 6), indicating that the proposed design is feasible. Such an obviously increased photocurrent of the CdS-WO_3@p-FTO photoelectrode probably was due to the efficient electron transfer and the charge separation in this composite, which can be attributed to the CdS-WO_3 Z-scheme heterostructure and the artificial PCs enhanced light absorption. The VBM of CdS is lower than the CBM of WO_3. The photoinduced electrons in the CBM of WO_3 migrate to the VBM of CdS through the CdS-WO_3 interface, which results in holes accumulating on the surface of WO_3 and the electrons accumulating on the surface of CdS. Further observation shows that the photocurrent of Z-scheme composite samples, CdS-WO_3@PCs-FTO and CdS-WO_3@p-FTO, are visibly higher than those of both pure WO_3@p-FTO and WO_3@PCs-FTO composites. A lower recombination rate and more efficient separation of photoinduced electron–hole pairs were exhibited by the CdS-WO_3 Z-scheme heterostructure. In addition, the photocurrent of the Z-scheme composite sample gradually decreases to zero when light is turned off because holes accumulated on the surface of WO_3 and the electrons accumulated on the surface of CdS are gradually released. With the assistance of PCs, the composites show higher photocurrents than those of composites without PCs. This effect is due to the high surface area of PCs, which enhanced the possibility of light absorption and provide more photoactive sites.

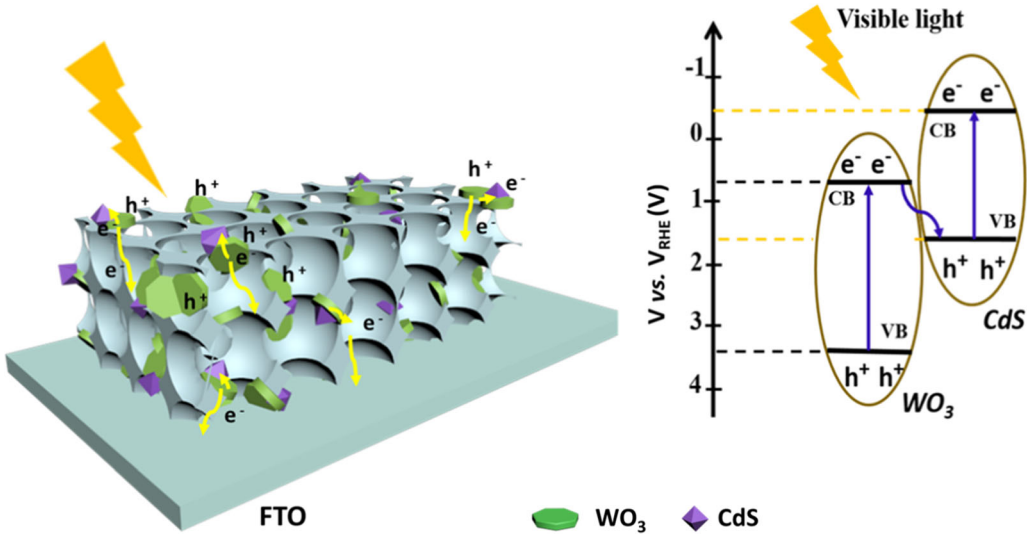

Fig. 5. Schematic diagram of the photocatalytic mechanism of Z-Scheme CdS-WO_3 heterostructure.

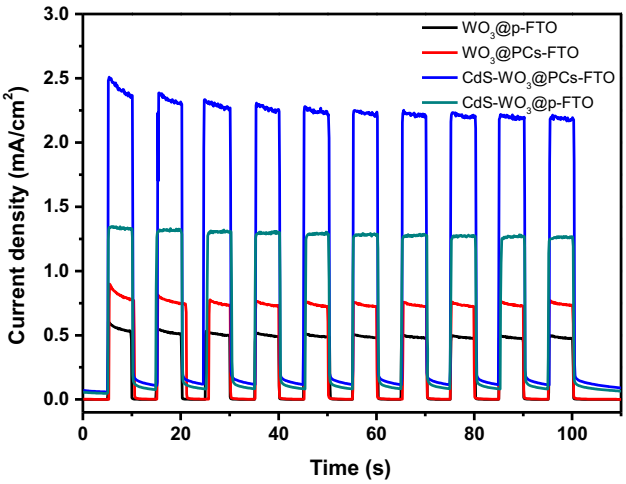

Fig. 6. Transient photocurrent responses of WO_3@p-FTO,WO_3@PCs-FTO, PCs-FTO, CdS-WO_3@PCs-FTO and CdS-WO_3@p-FTO at 0.4 V versus VAg/AgCl.

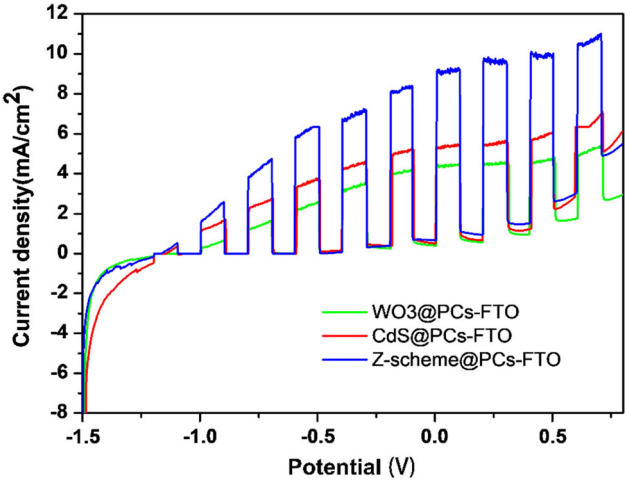

Fig. 7. LSV curves of WO_3@PCs-FTO, CdS@PCs-FTO and Z-scheme@PCs-FTO.

The transfer approaches of charge carriers were studied by linear sweep voltammetry (LSV) analysis under a chopped light. Figure 7 shows the LSV curves of WO_3@PCs-FTO, CdS@PCs-FTO, and CdS-WO_3@PCs-FTO, which show that the photo-generated current of CdS-WO_3@PCs-FTO was higher than the current of WO_3@PCs-FTO or CdS@PCs-FTO. Compared with WO_3@PCs-FTO and CdS@PCs-FTO, the Z-scheme CdS-WO_3 heterostructure can improve charge migration efficiency and accelerate the separation of electron–hole pairs.

Photocatalystic Degradation of RhB

The photocatalytic activity of Z-scheme CdS-WO_3@PCs-FTO was evaluated by the degradation of rhodamine B under a xenon lamp. Figure 8a shows the scheme of the degradation RhB solution with CdS-WO_3@PCs-FTO electrode (1 cm^2) under a 100 mW cm^{-2} xenon lamp; the RhB solution concentration is 0.1 mmol/L. The photo in Fig. 8b shows different shades of RhB solution from left to right after 0 min, 40 min, 80 min, 120 min, and 160 min illumination time. After 160 min of illumination, the RhB solution was almost transparent. Figure 8c depicts the UV–vis absorptance spectrum, which shows that the peaks of different curves do not change significantly. To clearly see the rate of degradation of the RhB solution with CdS-WO_3@PCs-FTO electrode under visible light, kinetically analyzed degradation of the RhB under illumination is shown in Fig. 8d. The results show a first-order kinetic reaction mechanism, the degradation constant k is 0.01571 min^{-1} and the R-square is 0.9445, which means the reaction rate is independent on the concentration of RhB.

Adding PCs powders to CdS-WO_3 heterojunction can degrade the solution completely in one hour[37]

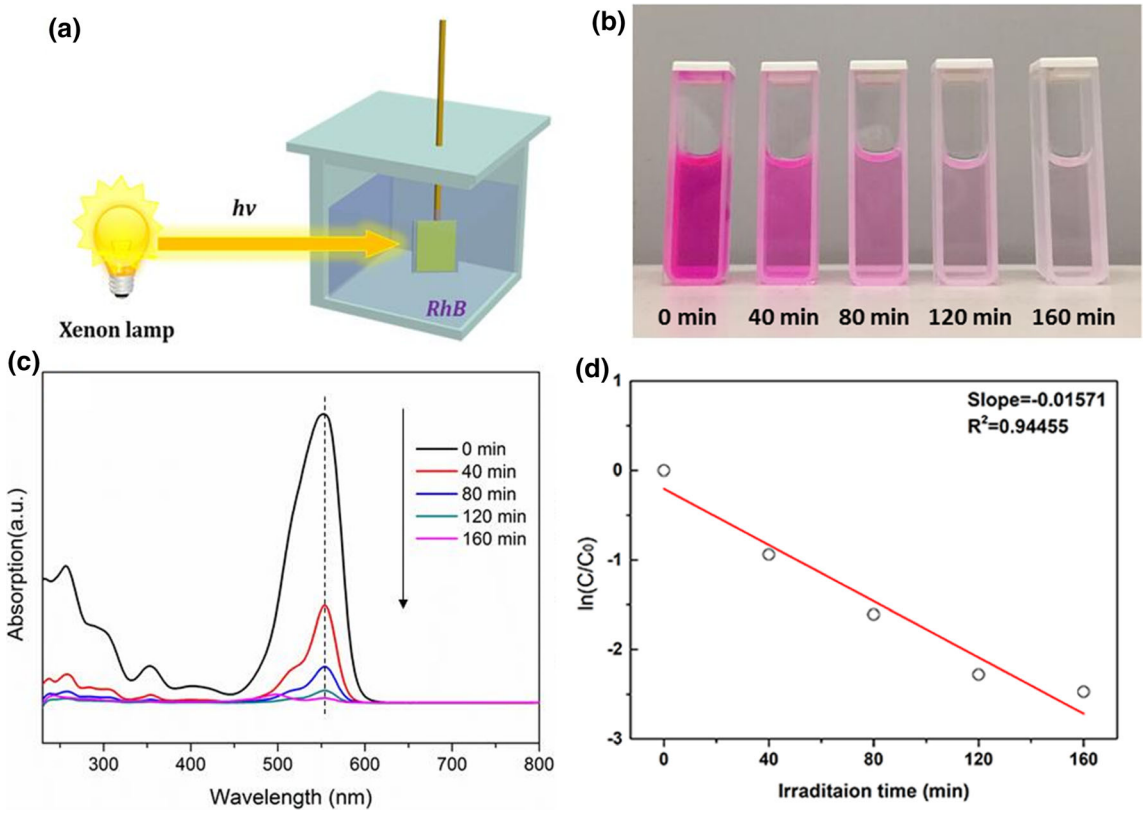

Fig. 8. (a) Scheme of the degradation of RhB on CdS-WO_3@PCs-FTO; (b) image of RhB solution after irradiation with CdS-WO_3@PCs-FTO in 0 min, 40 min, 80 min, 120 min and 160 min; (c) absorption spectra of the solution of Fig. 8b; (d) the data were obtained by recording the variations in the absorption band (554 nm) in the UV–visible spectra of RhB and analyzed in a first-order kinetics reaction mechanism.

Table I. Partial comparisons with other systems in transient photocurrent responses and degradation time of RhB

Materials	Transient photocurrent responses (mA/cm^2)	Degradation time of RhB (min)
CdS[32]	–	180
TiO_2[33]	–	200
$BiVO_4$[34]	–	270
P/g-C_3N_4[35]	0.004	–
YVO_4/g-C_3N_4[36]	0.003	–
α-Fe_2O_3[7]	1.7	–
Z-scheme CdS/WO_3 (this work)	2.3	160

(the photocatalyst content is 0.5 g L^{-1} and the solution concentration is 15 mg L^{-1}). In this work, the thin film content on the tested electrode is much less; it takes 160 min to fully degrade. Compared with other photocatalysis systems (Table I), the Z-scheme structure in this work has a considerably higher transient photocurrent response due to improved charge carrier separation, and the degradation time of the RhB is comparable with other systems. However, due to the integrity of the electrode compared with conventional powder samples, the recycling of the photo-active materials on a bulk electrode is far more convenient than that of powders suspended in an aqueous phase, which is more meaningful for large-scale applications.

CONCLUSIONS

In summary, WO_3@PCs-FTO was synthesized via a solvothermal method and by an in situ method. Attributed to the direct Z-scheme heterostructure of WO_3-CdS, photo-generated electrons and holes were separated effectively. It was found that WO_3-CdS@PCs-FTO showed largely improved photocatalytic activity compared with WO_3@PCs-FTO. In addition, photonic crystal FTO was used in the

photoanode because of its inverse opal structure, which can enhance light absorption. This work provided a potential way to improve the efficiency of photocatalytic performance of a photocatalyst and thus optimize the utilization of sunlight in the field of solar energy and solar cells.

ACKNOWLEDGMENTS

This work was supported by the National Natural Science Foundation of China (Grant No. 51602065).

CONFLICT OF INTEREST

The authors declare no conflict of interest.

ELECTRONIC SUPPLEMENTARY MATERIAL

The online version of this article (https://doi.org/10.1007/s11664-020-08244-1) contains supplementary material, which is available to authorized users.

REFERENCES

1. B. Zhang and L. Sun, *Chem. Soc. Rev.* 48, 2216 (2019).
2. N. Roy, N. Suzuki, C. Terashima, and A. Fujishima, *Bull. Chem. Soc. Jpn* 92, 178 (2019).
3. K. Pan, Y.Z. Dong, W. Zhou, Q.J. Pan, Y. Xie, T.F. Xie, G.H. Tian, and G.F. Wang, *ACS Appl. Mater. Interfaces* 5, 8314 (2013).
4. M.B. Tahir, *J. Inorg. Organomet. Polym Mater.* 28, 2160 (2018).
5. E.J. Joo, G. Park, J.S. Gwak, J.H. Seo, K.Y. Jang, K.H. Oh, and K.M. Nam, *J. Nanomater.* 2016, 1 (2016).
6. L.F. Li, X.L. Zhao, D.L. Pan, and G.S. Li, *Chin. J. Catal.* 38, 2132 (2017).
7. K. Maeda and T.E. Mallouk, *Bull. Chem. Soc. Jpn.* 92, 38 (2019).
8. Z. Wang, X. Li, H. Ling, C.K. Tan, L.P. Yeo, A.C. Grimsdale, and A.I.Y. Tok, *Small* 14, 1800395 (2018).
9. Y. Xiao, M.S. Chen, and M.L. Zhang, *ChemPhotoChem* 3, 101 (2019).
10. Y. Xiao, M.S. Chen, and M.L. Zhang, *J. Power Sources* 402, 62 (2018).
11. L. Huang, X.L. Wang, J.H. Yang, G. Liu, J.F. Han, and C. Li, *J. Phys. Chem. C* 117, 11584 (2013).
12. D. Sarkar, C.K. Ghosh, S. Mukherjee, and K.K. Chattopadhyay, *ACS Appl. Mater. Interfaces* 5, 331 (2013).
13. C. Liu, J.Y. Tang, H.M. Chen, B. Liu, and P.D. Yang, *Nano Lett.* 13, 2989 (2013).
14. X.W. Wang, G. Liu, Z.G. Chen, F. Li, L.Z. Wang, G.Q. Lu, and H.M. Cheng, *Chem. Commun.* 23, 3452 (2009).
15. Z.F. Liu, Z.G. Zhao, and M. Miyauchi, *J. Phys. Chem. C* 113, 17132 (2009).
16. C.D. Song, X. Wang, J. Zhang, X.B. Chen, and C. Li, *Appl. Surf. Sci.* 425, 788 (2017).
17. T.T. Xiao, Z. Tang, Y. Yang, L.Q. Tang, Y. Zhou, and Z.G. Zou, *Appl. Catal. B Environ.* 220, 417 (2018).
18. J.F. Zhang, S. Wageh, A.A. Ghamdi, and J.G. Yu, *Appl. Catal. B-Environ.* 192, 101 (2016).
19. Q. Li, X. Li, S. Wageh, A.A. Ghamdi, and J.G. Yu, *Adv. Energy Mater.* 5, 1500010 (2015).
20. S. Hong, D.P. Kumar, D.A. Reddy, J. Choi, and T.K. Kim, *Appl. Surf. Sci.* 396, 421 (2017).
21. A. Phuruangrat, D. Jin Ham, S.J. Hong, S. Thongtem, and J.S. Lee, *J. Mater. Chem.* 20, 1683 (2010).
22. V. Chakrapani, J. Thangala, and M.K. Sunkara, *Int. J. Hydrog. Energy* 34, 9050 (2009).
23. X.Q. Chen, J.H. Ye, S.X. Ouyang, T. Kako, Z.S. Li, and Z.G. Zou, *ACS Nano* 5, 4310 (2011).
24. X. Ke, M.M. Yang, W.Z. Wang, D.X. Luo, and M.L. Zhang, *Materials* 12, 2558 (2019).
25. T. Baba, *Nat. Photonics* 2, 465 (2008).
26. Z.Z. Yang, S.M. Gao, W. Li, V.V. Vitalii, U. Welp, W.K. Kwok, and T. Xu, *ACS Appl. Mater. Interfaces* 3, 1101 (2011).
27. Y. Gun, G.Y. Song, V.H.V. Quy, J. Heo, H. Lee, K.S. Ahn, and S.H. Kang, *ACS Appl. Mater. Interfaces* 7, 2029 (2015).
28. T.P. Hu, P.F. Li, J.F. Zhang, C.H. Liang, and K. Dai, *Appl. Surf. Sci.* 442, 20 (2018).
29. J. Jin, J.G. Yu, D.P. Guo, C. Cui, and W.K. Ho, *Small* 11, 5262 (2015).
30. L.J. Zhang, S. Li, B.K. Liu, D.J. Wang, and T.F. Xie, *ACS Catal.* 4, 3724 (2014).
31. M.L. Zhang, R.W. Mitchell, H.W. Huang, and R.E. Douthwaite, *J. Mater. Chem. A* 5, 22193 (2017).
32. B. Pan, Y. Xie, S. Zhang, L. Lv, and W. Zhang, *ACS Appl. Mater. Interfaces* 4, 3938 (2012).
33. T.S. Natarajan, M. Thomas, K. Natarajan, H.C. Bajaj, and R.J. Tayade, *Chem. Eng. J.* 169, 126 (2011).
34. W.W. He, X.F. Zhang, X.L. Dong, X.X. Zhang, C. Ma, and H.C. Ma, *J. Adv. Oxid. Technol.* 17, 33 (2014).
35. J.J. Feng, D.K. Zhang, H.P. Zhou, M.Y. Pi, X.D. Wang, and S.J. Chen, *ACS Sustain. Chem. Eng.* 6, 6342 (2018).
36. J. Cai, Y.M. He, X.X. Wang, L.H. Zhang, L.Z. Dong, H.J. Lin, L.H. Zhao, X.D. Yi, W.Z. Weng, and H.L. Wan, *RSC Adv.* 3, 20862 (2013).
37. D. Sengupta, P. Das, B. Mondal, and K. Mukherjee, *Renew. Sust. Energ. Rev.* 60, 356 (2016).

Publisher's Note Springer Nature remains neutral with regard to jurisdictional claims in published maps and institutional affiliations.